

Capturing Stable HDR Videos Using a Dual-Camera System

Qianyu Zhang, Bolun Zheng*, Hangjia Pan, Lingyu Zhu, Zunjie Zhu, Zongpeng Li, Shiqi Wang

Abstract—In HDR video reconstruction, exposure fluctuations in reference images from alternating exposure methods often result in flickering. To address this issue, we propose a dual-camera system (DCS) for HDR video acquisition, where one camera is assigned to capture consistent reference sequences, while the other is assigned to capture non-reference sequences for information supplementation. To tackle the challenges posed by video data, we introduce an exposure-adaptive fusion network (EAFNet) to achieve more robust results. EAFNet introduced a pre-alignment subnetwork to explore the influence of exposure, selectively emphasizing the valuable features across different exposure levels. Then, the enhanced features are fused by the asymmetric cross-feature fusion subnetwork, which explores reference-dominated attention maps to improve image fusion by aligning cross-scale features and performing cross-feature fusion. Finally, the reconstruction subnetwork adopts a DWT-based multiscale architecture to reduce ghosting artifacts and refine features at different resolutions. Extensive experimental evaluations demonstrate that the proposed method achieves state-of-the-art performance on different datasets, validating the great potential of the DCS in HDR video reconstruction. The codes and data captured by DCS will be available at <https://github.com/zqqqyu/DCS>.

Index Terms—HDR video, dual-camera system, multi-exposure image fusion

I. INTRODUCTION

CAPTURING the full range of illumination in high dynamic range (HDR) scenarios is a challenging task for standard digital cameras [1], [2]. Thanks to the multi-exposure fusion (MEF) technology [3]–[5], we can successfully capture HDR images in static scenarios by fusing multiple images of different exposure times. However, capturing HDR videos with a standard digital camera in dynamic scenes has not yet been effectively resolved. Early studies concentrated on designing hardware systems for directly capturing HDR video, including internal/external beam splitters [6]–[8], specialized sensors [9], [10], modulo cameras [11] and neuromorphic cameras [12], etc. Although these solutions show good potential for capturing high-quality HDR videos, their high cost and bulky design severely limit their widespread adoption.

To address the limitations of these issues, researchers [13]–[15] have turned to computational methods that leverage inexpensive standard digital cameras, providing a promising direction for HDR video reconstruction. With the rapid advancement of deep learning, researchers make efforts to solve HDR imaging problems in dynamic scenes with deep neural networks. These methods can be broadly categorized into two

Qianyu Zhang, Bolun Zheng, Hangjia Pan, Zongpeng Li are with the School of Automation, Hangzhou Dianzi University, Hangzhou 310018, China (e-mail: qyzhang@hdu.edu.cn; blzheng@hdu.edu.cn; 1072272964@qq.com; zongpeng@tsinghua.edu.cn), Zunjie Zhu is with the Lishui Institute of Hangzhou Dianzi University (e-mail: zunjie.zhu@hdu.edu.cn), Lingyu Zhu and Shiqi Wang are with the Department of Computer Science, City University of Hong Kong (e-mail: lingyuzhu-c@my.cityu.edu.hk; shiqi.wang@cityu.edu.hk)

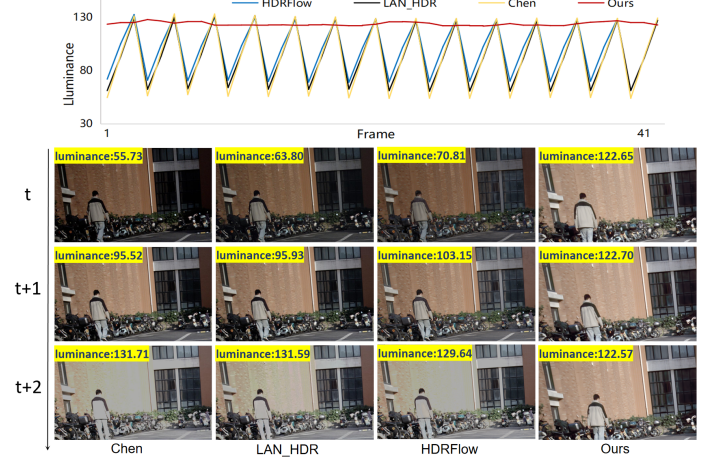


Fig. 1. Qualitative comparison between SAFNet and AE methods. Existing AE methods result in flickering artifacts (luminance fluctuations exceeding 30). In contrast, our system ensures consistent illumination across reference frames, enabling temporally consistent HDR reconstruction results (luminance fluctuations limited to under 1).

types. One approach follows the MEF attempts, aiming to reconstruct an HDR image by fusing misaligned multi-exposure images. They typically use a specific exposure image as a reference frame for HDR reconstruction. As a result, capturing HDR video using these methods often requires a large number of additional exposure images, making it difficult to meet the real-time requirements of video capture. To overcome this limitation, alternating exposure (AE) methods [16]–[20] have been proposed, which allow varying exposures as reference frames and eliminate the need for additional exposure images. However, aligning the brightness of reference frames of different exposures and achieving consistent and stable lighting in the reconstruction video is still challenging. Although existing AE methods have achieved excellent performance on public benchmarks, they struggle to handle complex real-world scenes and lighting variations (shown in Fig. 1).

Generally, both existing MEF methods and AE methods struggle to achieve high-quality video capture in dynamic scenes. Compared to AE methods, MEF methods could produce HDR image sequences with stable and consistent lighting because of their use of a fixed-exposure reference. Noticing the wide use of multi-camera system in consumer electronic devices, it is possible to introduce multi-camera system for high-quality HDR video capture. Based on these insights, we develop a dual-camera system (DCS) for capturing high-quality HDR videos. In the DCS, one camera is assigned to capture reference images, while the other is assigned to capture non-reference images for MEF. In this way, the DCS could effectively mitigate the temporal inconsistencies associated with AE methods while avoiding the acquisition

latency inherent in MEF.

Within DCS, HDR video reconstruction with MEF faces greater challenges than static images for two main reasons. First, exposures of input frames become uncertain. Second, the backgrounds from non-reference images are no longer aligned with the reference frame. Existing MEF methods can be categorized into two main approaches: optical-flow-based and attention-based. The former relies on optical flow to align inputs before fusion, which often suffers from a low accuracy in estimating optical flow. On the other hand, attention-based methods, while offering greater flexibility, mainly depend on the quality of the attention maps for fusion. Therefore, existing attention-based MEF methods encounter two main issues in reconstructing HDR videos within DCS. First, they fail to adequately leverage exposure information, relying primarily on texture and luminance to calculate attention maps, which may suffer from the various exposure settings. Second, they hardly consider the importance of reference frames, particularly in the computation of attention maps, where equal weights are often assigned to both reference and non-reference frames. This leads to attention being skewed by non-reference inputs, especially in complex, dynamic scenes, thereby hindering the effective elimination of artifacts.

Against the above limitations, we propose an exposure-adaptive fusion network (EAFNet) to achieve robust and generalized HDR reconstruction. Our EAFNet consists of a pre-alignment subnetwork, an asymmetric cross-feature fusion subnetwork, and a reconstruction subnetwork. The pre-alignment subnetwork consists of a global luminance alignment (GLA) and an exposure-guided feature selection module (EFSM) to leverage exposure information, enhancing meaningful details and ensuring that the most relevant features are preserved despite varying exposure levels. The asymmetric cross-feature fusion subnetwork aims to explore reference-dominated attention maps, align cross-scale features, and integrate cross-feature information to improve the fusion. Additionally, a multiscale reconstruction subnetwork is introduced to suppress ghosting artifacts and enhance fine details. Summary, our contributions can be summarized as follows:

- We propose a new HDR video generation paradigm that uses a fixed medium-exposure sequence as the temporal reference, while leveraging a second varying-exposure stream to enrich dynamic range. This design fundamentally improves temporal consistency and reconstruction stability.
- We designed and implemented an asynchronous dual-camera system to validate the feasibility of our proposed paradigm and bridge the gap between algorithmic design and practical deployment. Furthermore, existing MEF methods can be seamlessly applied within our system, achieving temporally consistent reconstruction.
- Built upon MEF methods, we propose a novel model design, EAFNet. The proposed pre-alignment subnetwork leverages exposure information and explores the intrinsic properties of the images, ensuring that the most relevant features receive attention despite varying exposure levels. An asymmetric cross-feature fusion subnetwork is introduced to explore reference-dominated attention maps,

achieving smoother and more consistent fusion through cross-scale alignment and cross-feature interaction.

- Our EAFNet achieves state-of-the-art results on public benchmarks. Both qualitative and quantitative experiments demonstrate the effectiveness of our EAFNet and DCS.

II. RELATED WORK

A. HDR Image Reconstruction.

1) *Traditional Methods.*: Traditional multi-exposure image fusion HDR imaging methods usually solve the ghosting problem in the image domain, and currently there are two main types of solutions:

Motion-aligned-based. These methods focus on a global alignment of the LDR input and then reject the unaligned pixels before image fusion to achieve de-ghosting. Bogoni *et al.* [4] used optical flow to estimate motion vectors between LDR images and warp the moving pixels accordingly. Kang *et al.* [16] improved the alignment results by using the exposure time information to transform the intensity of LDR images to the brightness domain before aligning them with the optical flow method. Sen *et al.* [5] proposed a patch-based energy minimization method that integrates alignment and HDR reconstruction into a joint optimization. Hu *et al.* [21] optimized alignment using luminance and gradient consistency in the transform domain. Hafer *et al.* [22] proposed an energy minimization approach to jointly compute HDR radiance and displacement fields. These motion-alignment methods heavily rely on the accuracy of the alignment algorithms.

Motion-rejection-based. Motion-rejection methods detect and exclude motion regions before fusion. Grosch *et al.* [23] identified motion regions based on intensity differences, while Jacobs *et al.* [13] used weighted variance to detect ghosting. He *et al.* [24] refined motion detection by combining joint probability density with graph-cut-based energy minimization. Zhang *et al.* [25] removed motion pixels using image gradient information, while Lee *et al.* [26] and Oh *et al.* [27] introduced rank minimization to detect motion and reconstruct HDR images. However, discarding motion regions often compromises information recovery in static areas.

2) *Deep Learning Approaches.*: With the rapid advancement of deep learning, neural network-based methods for HDR image reconstruction have gained significant attention and have emerged as the prevailing approach in the field, these can be categorized primarily into the following types:

Flow-based Alignment. Kalantari *et al.* [28] first applied CNNs to multi-exposure HDR imaging, using optical flow to register non-reference LDR images to a reference image. Since LDR images contain not only motion regions but also saturated regions, which do not satisfy the assumption of luminance consistency of the optical flow method, Peng *et al.* [29] and Prabhakar *et al.* [30] suggested that the typical optical flow algorithm may lead to large misalignment errors. Therefore, they used optical flow networks (e.g., FlowNet) to achieve alignment. SAFNet [31] refined valuable regions and estimated motion to produce high-quality HDR images. However, when long-distance motions occur in the LDR images, these methods still struggle to estimate the accurate flow for alignment.

Direct Feature Concatenation. Wu *et al.* [32] introduced a flow-free approach, treating HDR imaging as an image transformation problem. They first applied homography to align multiple frames globally and then used a multiscale network to map LDR images to HDR images directly. A similar approach was also employed in [33]. Niu *et al.* [34] and Li *et al.* [35] used Generative Adversarial Networks (GANs) for HDR reconstruction from multi-exposure LDR images with significant motion. However, they still face challenges in handling extreme motion and dynamic scenes.

Attention-based Alignment. AHDRNet [36] introduced the attention mechanism into multi-exposure HDR reconstruction for dynamic scenes, coupling it with a densely connected dilated residual module to achieve alignment and fusion. Liu *et al.* [37] introduced a Pyramid Cascading Deformable (PCD) module, using multiscale deformable convolutions for feature alignment in LDR images. Chen *et al.* [38] proposed novel attention mechanisms and progressive texture fusion to improve reconstruction. DomainPlus [39] utilized multiscale attention with fronted fusion to perform coarse-to-fine fusion. HDR-Trans *et al.* [40] added Transformer to the CNN-based HDR architecture, combining the advantages of CNN in extracting local information and Transformer in capturing global information. Chen *et al.* [41] proposed a transformer model for HDR imaging with three steps: alignment, fusion, and reconstruction. Yan *et al.* [42] proposed a HyHDRNet consisting of a content alignment subnetwork and a transformer-based fusion subnetwork to improve performance. SCTNet [43] integrated spatial and channel attention in a transformer-based network to improve semantic coherence. Despite advances in these approaches, they still generate undesirable ghosts in high-contrast regions.

3) *Dual-lens-based system:* Dual-lens HDR imaging leverages paired images with different exposures to synthesize high-quality HDR content. Dong *et al.* [44] employ a soft-warping step to align long-exposure features to the short-exposure reference, Li *et al.* [45] propose a dual-stage model: a guided 3D exposure correction network estimates a coarse HDR image from the short exposure input, followed by a guided denoising transformer that refines the result using long-exposure features. While effective under controlled conditions, both frameworks assume the only misalignment present is 1D parallax between image pairs. This assumption is embedded in their data collection and rectification procedures, simplifying alignment to left-right disparities but limiting their ability to model more complex distortions. In dynamic scenes, exposure time mismatch introduces additional misalignments: high-exposure frames exhibit motion blur not present in low-exposure frames.

B. HDR Video Reconstruction

Dedicated Hardware Solutions. Dedicated hardware solutions, such as single-pixel imaging [46], scanline exposure/ISO [9], internal [8] or external beam splitters [7], as well as residue cameras [11] and neuromorphic vision cameras [12], are capable of rapidly and efficiently generating detailed HDR images or videos on specialized devices. However, the

complexity and high cost of these hardware solutions limit their widespread adoption.

Traditional Methods. Similar to multi-exposure HDR image fusion, most methods utilize alternating exposure sequences to align multiple frames for HDR video reconstruction. Kang *et al.* [16] introduced the first algorithm in this category, employing global and local registration to align multi-exposure images at each time step and merge them into a single HDR frame. Kalantari *et al.* [17] employed patch-based optimization to reconstruct missing images from different exposures. Mangiat *et al.* [17] applied block-based motion estimation with refined motion vectors and later improved this method with HDR filtering to eliminate block artifacts [47]. Additionally, Gryaditskaya *et al.* [18] proposed an adaptive weighting algorithm to minimize motion artifacts. Li *et al.* [48] proposed a statistical method to avoid exact alignment estimation. However, these methods are typically time-consuming and often introduce visible artifacts.

Deep Learning Methods. Kalantari *et al.* [49] proposed the first deep learning-based method for generating HDR video from alternating exposure sequences. Chen *et al.* [19] developed a two-stage coarse-to-fine framework that integrated deformable convolutions with HDR video reconstruction. LAN-HDR [50] aligned adjacent frames with the reference frame using luminance-based attention scores. HDRFlow [51] designed an efficient flow network with multiscale large kernels to handle large motions. Cui *et al.* [20] introduced exposure completion for neural HDR rendering, using feature interpolation and a novel decoding architecture to improve HDR video reconstruction. Nonetheless, the varying exposures of the reference frames create a significant challenge in maintaining temporal consistency in video reconstruction.

III. DUAL-CAMERA SYSTEM FOR HDR VIDEO

Overview. A mainstream solution for HDR video reconstruction is generating video from image sequences captured at alternating exposure levels. However, this approach inherits the exposure limitations of the reference frame, often resulting in visible artifacts and temporal flickering in the generated video, significantly constraining its practical application. To address this, we propose a dual-camera system (As shown in Fig. 2 (b)), where the primary camera continuously captures medium-exposure images to ensure temporal consistency, while the secondary camera captures low-exposure and high-exposure images to provide complementary information.

A. Dual-Camera System

System Configuration. Our system employs two MV-CS032-10GC industrial cameras, which provide low-level access to operational controls for precise adjustment of exposure time and shooting strategies. Both cameras are equipped with identical lenses and are mounted side by side, secured by a mechanical support structure to ensure their relative positions remain stable throughout the imaging process.

Dual-Camera Calibration. To eliminate distortion and ensure alignment, we perform camera calibration using a checkerboard pattern. Intrinsic and extrinsic parameters are computed

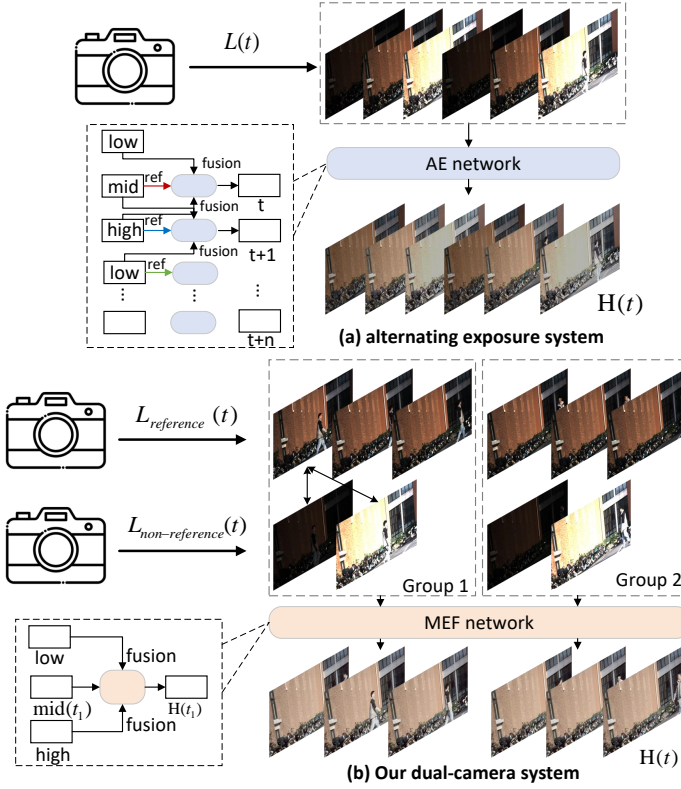


Fig. 2. Visualization of our dual-camera system. The primary camera captures continuous medium-exposure sequences as reference for temporal consistency, while the secondary camera alternates between low- and high-exposure to provide complementary information for reconstruction.

from images captured by the dual cameras using the camera calibration toolbox [52]. The calibration parameters are then applied to register the images, resulting in the final aligned images. This reduces potential errors and improves the subsequent processing steps.

Video Capture. Both cameras are triggered to start capturing images simultaneously, but subsequent image capture can occur asynchronously. One camera captures the medium-exposure reference sequence $L_{reference}(t)$, while the other captures the alternating exposure non-reference sequence $L_{non-reference}(t)$ with low and high exposure. Both cameras are set to the same resolution of $w \times h$. Due to different exposure time settings, the videos captured by the two cameras are not timestamp-synchronized. However, our method does not require precise synchronization. We use timestamp information to roughly group the data, where each group consists of frames from $L_{reference}(t)$ and two high- and low-exposure images from $L_{non-reference}(t)$ (e.g., with exposure times of $(-2, 0, 2 \text{ EV})$, every four frames from the reference sequence, along with one pair of high- and low-exposure images, form a single group). Each frame, along with the two high- and low-exposure images, is used as input to the network. The final reconstructed HDR video matches the frame rate of $L_{reference}(t)$. To ensure a fair comparison, we capture test datasets for both AE and MEF using our system. Detailed information can be found in Sec. V-B, and the datasets will be available.

Essentially, our system can be viewed as a multi-exposure HDR fusion task for dynamic scenes, where luminance alignment between neighboring frames is unnecessary due to consistently exposed reference frames. Existing MEF methods can be seamlessly extended to achieve consistent exposure results. To address challenges from video data and the variability of real-world scenes, we propose SAFNet, a more robust network, detailed in Section IV.

B. Discussion.

The proposed DCS offers several advantages over traditional single-camera AE methods for HDR video reconstruction:

Stable Lighting Conditions. The DCS provides more stable exposure across frames, avoiding the fluctuations typical in alternating exposure systems.

Potential in Low-Light Conditions. The DCS performs better in low-light environments, where long exposure times in a single-camera setup can lead to artifacts and delays. The dual-camera approach mitigates these issues by distributing exposure tasks between the cameras.

Offline HDR Video Reconstruction. The DCS setup supports offline HDR video reconstruction, allowing continuous high-quality video capture without real-time processing, ensuring high-quality capture without real-time processing delays. In contrast, AE methods require real-time reconstruction to avoid flickering, which can introduce undesirable artifacts if not processed immediately.

Independent Automatic Exposure. Each camera in the DCS can independently apply established automatic exposure strategies, eliminating the need for recalibration with each frame and simplifying real-time operation. In contrast, AE methods require constant adjustments to exposure settings, complicating real-time capture.

Seamless Integration with Encoding Strategies. The dual-camera framework integrates easily with existing video encoding and decoding strategies. The secondary camera can capture frames at a low frame rate (e.g., 1fps or lower), minimizing additional bandwidth requirements, thus ensuring efficient video transmission.

IV. METHOD

A. Overview

Given a set of LDR images of a dynamic scene $\{L_1, L_2, \dots, L_n\}$ with different exposures, HDR imaging aims to generate an HDR image H aligned to a prescribed reference image. Fig. 3 shows an overview of the proposed EAFNet. Our proposed EAFNet consists of three main subnetworks: the pre-alignment subnetwork, the asymmetric cross-feature fusion subnetwork, and the restoration subnetwork.

B. Pre-alignment

The pre-alignment subnetwork aims to extract meaningful details from the non-reference image by leveraging exposure information. Global luminance alignment (GLA) is introduced to maintain consistent luminance across varying exposures, while the exposure-guide feature selection module (EFSM)

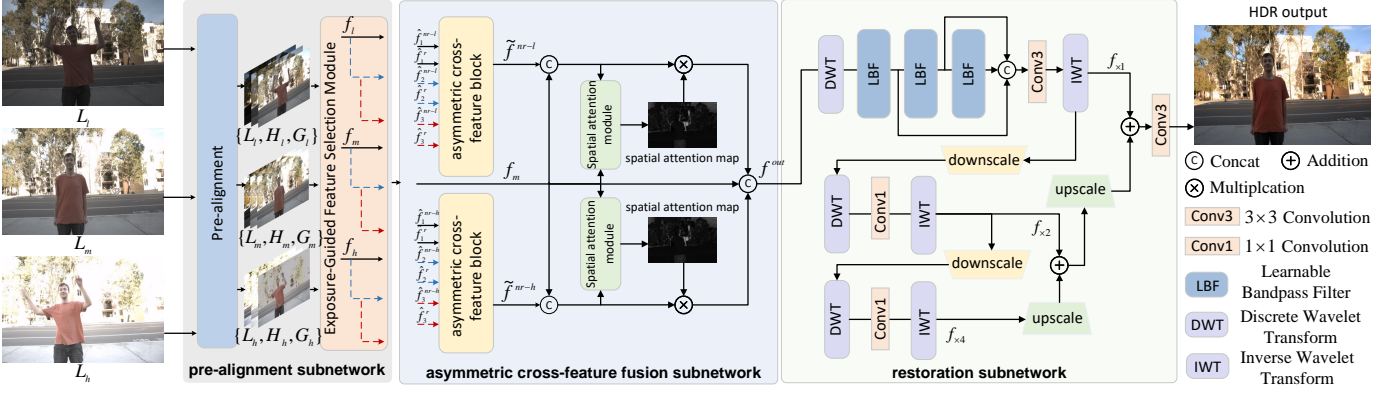


Fig. 3. The architecture of EAFNet consists of a pre-alignment subnetwork, an asymmetric cross-feature fusion subnetwork, and a restoration subnetwork. We introduce GLA and EFSM to leverage exposure information, explore the intrinsic properties of the images, and help preserve finer details across varying exposures. The asymmetric cross-feature fusion subnetwork improves image fusion by aligning cross-scale features and performing cross-feature fusion. The reconstruction subnetwork adopts a DWT-based multiscale architecture to reduce ghosting and refine features at different resolutions.

explores the correlation between inputs and exposure to focus on the most relevant regions for fusion.

Global Luminance Alignment. Following [36], [53], we employ three LDR images $\{L_l, L_m, L_h\}$ (sorted by their exposure length) as input. The images first undergo gamma correction [53], defined as:

$$H_i = L_i^\gamma / t_i, \quad i = l, m, h \quad (1)$$

where $\gamma > 1$ denotes the gamma correction parameter and t_i denotes the exposure time. The indices l, m, h correspond to low, mid, and high exposure settings, respectively, with m serving as the reference image. In this work, the default gamma parameter γ is set to 2.2. Then, we will get a corresponding set of $\{H_i\}$.

Due to varying luminance levels at different exposure times, captured images may exhibit color rendering deviations from real-world colors, with low-exposure images losing shadow details and high-exposure images losing highlight details. Therefore, variations in exposure times certainly affect the overall color accuracy of the input LDR images. To address this, we propose a GLA in the pre-alignment subnetwork. GLA aims to correct the luminance of LDR images in the sRGB domain, producing consistent brightness features across varying exposures and enhancing detail preservation. Specifically, the LDR images are mapped to the luminance range of the reference image and achieve global luminance alignment:

$$G_i = \text{clip}(L_i * (\text{mean}(L_i) / \text{mean}(L_m))), \quad i = l, h) \quad (2)$$

where G_i denotes the corresponding luminance-aligned output, $\text{mean}(\cdot)$ denotes the mean luminance value, and clip is a function that keeps the output in the range $[0, 1]$. Notably, since L_m is the reference image, $G_m = L_m$.

As shown in Fig. 4, given a set of LDR images with varying exposure times, the non-reference images can be aligned to the reference image using GLA. Finally, we can obtain 3-pairs of 9-channel tensor $L_{in} = (\{L_l, H_l, G_l\}, \{L_m, H_m, G_m\}, \{L_h, H_h, G_h\})$ as the input to feed into the EFSM module.

Exposure-Guided Feature Selection Module. Existing methods primarily focus on texture for fusion, overlooking the

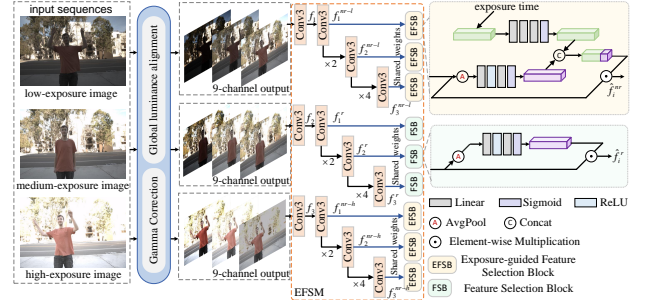


Fig. 4. The pre-alignment subnetwork is composed of two parts: global luminance alignment (GLA) and exposure-guided feature selection module (EFSM). The input is divided into multiple scales using a 3×3 convolution, with a shared-weight feature selection block applied at each scale.

crucial role of exposure time information, which may result in suboptimal fusion and color inconsistencies. To overcome this limitation, we propose an EFSM to explore exposure information, enhancing meaningful details and ensuring that the most relevant features are preserved despite varying exposure levels.

For a set of LDR images with corresponding exposure times of $\{t_l, t_m, t_h\}$, we standardize and relativize the input exposure times using the following formulation:

$$e_l = \log_2(t_l/t_m) \cdot c, \quad e_h = \log_2(t_h/t_m) \cdot c \quad (3)$$

where e_l and e_h denote the relative exposure inputs of the low exposure branch and high exposure branch, respectively. c is the hyper-parameter set to 0.1.

As shown in Fig. 4, we adopt a multiscale architecture to progressively refine feature representations across different exposure levels. The framework initiates with multi-level feature extraction: given input L_{in} , three parallel 3×3 convolutional layers generate initial feature maps $\{f_l, f_m, f_h\}$ corresponding to low-, mid-, and high-exposure features, respectively. For subsequent processing clarity, we formally define $f^{nr} \triangleq \{f_l, f_h\}$ as non-reference features and $f^r \triangleq f_m$ as reference features. Assuming there are N scales in total, the reference and non-reference features of the i -th scales are denoted as f_i^r and f_i^{nr} , respectively ($i = 1$ denotes the original scale), f_i^{nr}

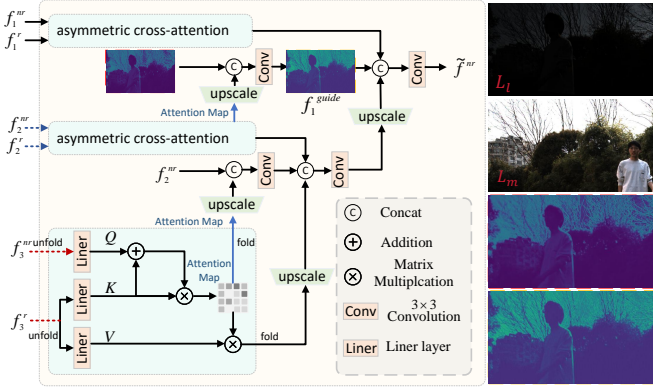


Fig. 5. The structure of asymmetric cross-feature block. It employs asymmetric cross-attention to align reference and non-reference features, integrating coarse-to-fine guidance for enhanced reference-dominated feature fusion and improved HDR reconstruction.

are fed to the shared weights exposure-guided feature selection block (EFSB) and f_i^r are fed to the shared weights feature selection block (FSB). Specifically, the features undergo global average pooling, followed by two fully connected layers and a sigmoid activation to produce the feature-guide modulation coefficients $v^{nr} \in \mathbb{R}^{1 \times 1 \times 64}$ and $v^r \in \mathbb{R}^{1 \times 1 \times 64}$. Simultaneously, relative exposure inputs e are each passed through fully connected layers, resulting in the exposure-guide modulation coefficients $v^t \in \mathbb{R}^{1 \times 1 \times 128}$.

To dynamically select and refine features from multiple input channels, the exposure-guide modulation coefficients $u^{nr} \in \mathbb{R}^{1 \times 1 \times 64}$ are computed as follows:

$$u^{nr} = \sigma(FC_3(<v^{nr}, v^t>)) \quad (4)$$

where $<, >$ denotes concatenation, σ represents sigmoid activation, FC_3 denotes three fully connected layers. The final output of EFSM can be obtained as:

$$\hat{f}_i^r = f_i^r \cdot v^r, \quad \hat{f}_i^{nr} = f_i^{nr} \cdot u^{nr} \quad (5)$$

C. Asymmetric Cross-feature Fusion

While the non-reference image may provide more details, it also poses a higher risk of introducing ghosting artifacts, especially in open scenes. To address this, we propose an asymmetric cross-attention block, which enhances the contribution of the reference input during attention computation and mitigates the potential for ghosting artifacts.

Generally, we propose a multi-scale strategy to calculate the attention in a coarse-to-fine manner. At each scale, asymmetric cross-attention (ACA) is utilized to compute local attention. Specifically, as shown in Fig. 5, the proposed ACA first utilizes the non-reference feature as an agent, facilitating the exchange of information between the patch tokens of the reference feature and then back project it to its non-reference branch. To prioritize mid-exposure image features and encourage more effective exploration of feature interactions across different exposures, we introduce the self-information during the exchange

process. Following [54], the attention matrix is thus computed as follows:

$$Q_i = \phi(\hat{f}_i^r)W_i^q, \quad K_i = \phi(\hat{f}_i^{nr})W_i^k, \quad V_i = \phi(\hat{f}_i^{nr})W_i^v \quad (6)$$

$$A_i = \text{softmax}((Q_i + K_i)K_i^T / \sqrt{C}) \quad (7)$$

where $W_i^q, W_i^k, W_i^v \in \mathbb{R}^{C \times C}$ are learnable weight matrices of the i -th scales, $\phi(\cdot) \in \mathbb{R}^{N \times C}$ denotes the unfolding operation (N refers to the number of patches). Then, the aligned non-reference features f_i^{anr} are obtained by applying a folding operation to the result of the multiplication of A_i and V_i .

To leverage attention from coarser scales and local details at the current scale, we introduce the cross-scale guidance feature f_i^{guid} to achieve coarse-to-fine feature fusion and interaction:

$$f_i^{guid} = C_v(<f_i^{nr}, U(\psi(A_{i+1} >))>), \quad 1 \leq I < N \quad (8)$$

where f_i^{guid} represent guidance features at i -th scales, U represents pixel shuffle upsampling, C_v denotes a 3×3 convolution. As shown in Fig. 5, f_i^{guid} learn reference-dominated attention from the previous scale, facilitating the alignment of features across scales. The output of asymmetric cross-attention block can be expressed as:

$$\tilde{f}^{nr} = C_v(<f_1^{anr}, U(f_2^{anr}), f_1^{guid}>) \quad (9)$$

Finally, we generate a spatial attention map with \tilde{f}^{nr} and f^r and get the final output:

$$f^{out} = <\sigma(C_v(\text{Relu}(C_v(<f^r, \tilde{f}^{nr}>)))) \cdot \tilde{f}^{nr}, f_m > \quad (10)$$

D. Restoration

The restoration subnetwork adopts a frequency-based approach to effectively mitigate ghosting artifacts in HDR images. As shown in Fig. 3, the subnetwork is designed with a multiscale architecture that progressively refines features at different resolutions. The architecture particularly emphasizes feature correction at lower scales, as these scales capture finer high-frequency details, such as textures and small features, which are essential for addressing the residual ghosting artifacts.

At the lower scales, the features undergo Discrete Wavelet Transform (DWT) to decompose the image into multi-resolution subbands. Following this, multiple Learnable Band-pass Filter (LBF) modules [39], [55] are applied to correct each frequency component. The output is then passed through the Inverse Wavelet Transform (IWT) to reconstruct the feature maps $f_{\times 1}$ in the feature domain. At higher scales, after applying DWT, a 1×1 convolution is used instead of multiple LBF modules. The feature maps at higher scales primarily contain global structural information, reducing the need for complex high-frequency corrections.

Finally, we combine the high-frequency details from lower scales with the global information from higher scales, leading to improved HDR image restoration with reduced ghosting artifacts:

$$H_{out} = \sigma(\text{Conv}(U(U(f_{\times 4}) + f_{\times 2}) + f_{\times 1})) \quad (11)$$

where U denotes upsampling, $f_{\times 4}, f_{\times 2}, f_{\times 1}$ are the output features at different scales, H_{out} represents the final HDR image output.

E. Loss Function

HDR images are typically displayed after tone mapping. To enhance training performance, we apply the μ -law transformation, as proposed in [28], to map the HDR image from the linear domain to the tone-mapped domain, thereby improving model performance during training, the μ -law transformation can be expressed as:

$$\tau(H) = \frac{\ln(1 + \mu H)}{\ln(1 + \mu)} \quad (12)$$

where μ is a hyperparameter set to 5000.

We adopt the L1 loss as the basic loss function for pixel-wise supervision. To correct each frequency component and enhance the training of the restoration subnetwork, we adopt the dilated advanced Sobel loss (D-ASL) loss function [56] as an additional function, which is defined as:

$$\mathcal{ASL}(\hat{Z}, Z) = \frac{1}{N} \sum |\text{Sobel}^*(\hat{Z}) - \text{Sobel}^*(Z)| \quad (13)$$

$$\mathcal{D} - \mathcal{ASL}^{\{d_1, d_2, \dots, d_n\}} = \sum_{i=1}^n \mathcal{ASL}|_{\text{dilation_rate}=d_i} \quad (14)$$

where the N is the batchsize of training, Z and \hat{Z} represent the groundtruth and the output image predicted by network after the μ -law function, Sobel^* denotes the advanced sobel filtering, and $\mathcal{ASL}|_{\text{dilation_rate}=d_i}$ denotes the ASL with a dilation rate of d_i . Following [56], we apply the reference settings that $D = \{1, 2, 3\}$ to formulate the D-ASL. Then the final loss function can be expressed as:

$$\text{Loss}(\hat{Z}, Z) = \mathcal{L}1(\hat{Z}, Z) + \lambda \cdot \mathcal{D} - \mathcal{ASL}^D(\hat{Z}, Z) \quad (15)$$

where $\lambda = 0.25$ is a hyper-parameter to balance the L1 loss and D-ASL.

V. EXPERIMENTS

1) *Settings*: The proposed method is implemented in PyTorch on an NVIDIA RTX4090 GPU. For the convolutional layers, we employ 64 kernels of size 3×3 with a stride of one, applying zero padding to preserve the dimensions of the resulting feature maps. The optimization is performed using the Adam optimizer [57] with an initial learning rate of 10^{-4} , and the training concludes when the learning rate reaches 10^{-6} . To train the model, both the LDR and corresponding images are cropped into 256×256 patches. A batch size of 16 is utilized during training. Patches are randomly rotated for data augmentation to avoid overfitting during the training stage.

TABLE I
COMPARISON RESULTS ON KALANTARI'S DATASET AND PRABHAKAR'S DATASET. THE BEST RESULTS ARE HIGHLIGHTED AND THE SECOND BEST RESULTS ARE UNDERLINED.

Models	17'CGF Kalantari	19'CVPR AHDRNet	20'ECCV Prabhakar	22'ECCV HDR-Trans	22'MM DomainPlus	23'ICCV SCTNet	24'ECCV SAFNet	Ours
train and test on Kalantari's dataset								
PSNR- μ	42.74	43.77	43.08	44.28	44.02	44.13	<u>44.61</u>	44.69
PSNR-L	41.22	41.35	41.68	<u>42.88</u>	41.28	42.12	43.09	42.19
SSIM- μ	0.9877	0.9907	/	0.9916	0.9910	0.9916	<u>0.9918</u>	0.9920
SSIM-L	0.9848	0.9859	/	0.9884	0.9864	0.9890	<u>0.9892</u>	0.9895
HDR-VDP-2	60.51	62.30	62.21	66.03	62.91	66.65	<u>66.93</u>	68.35
train and test on Prabhakar's dataset								
PSNR- μ	35.63	38.61	38.30	<u>41.31</u>	40.38	41.23	40.18	41.80
PSNR-L	32.50	35.26	34.98	39.44	38.08	38.75	37.90	40.13
SSIM- μ	0.9613	0.9663	0.9702	<u>0.9726</u>	0.9698	0.9724	0.9705	0.9731
SSIM-L	0.9692	0.9794	0.9781	<u>0.9885</u>	0.9872	0.9881	0.9865	0.9895
HDR-VDP-2	59.42	61.14	/	<u>63.01</u>	62.12	62.29	62.04	63.53

2) *Datasets*: We employ four benchmark datasets for evaluation: Prabhakar's dataset [30], Kalantari's dataset [28], Tursun's dataset [58] and Sen's dataset [5]. Details of these datasets are described as follows:

1). **Prabhakar's Dataset**. Including 582 varying exposure images with corresponding deghosted HDR images, with exposure values between -3EV to +3EV.

2). **Kalantari's dataset**. Including 74 training samples and 15 testing samples. Each consists of three LDR images, and the exposure values belong to $\{-2, 0, +2\}$ or $\{-3, 0, +3\}$.

3). **Tursun's dataset and Sen's dataset**. Lacking ground truth, is used to assess the generalization ability of the models.

3) *Metrics*: We quantitatively evaluate the predicted HDR images by measuring PSNR and SSIM [59] in both the linear domain (-L) and the tone-mapped domain ($-\mu$) [28]. The tone mapping operation is described in Sec. IV-E. Additionally, we compare the results using HDR-VDP-2 [60] for conforming the human visual perception. We also quantitatively evaluated the luminance consistency of the video by testing the Luminance Standard Deviation (LSD), temporal SSIM (t-SSIM) and average luminance (L_{avg}):

- Average Luminance (L_{avg}):

$$L_{avg} = \frac{1}{N} \sum_{i=1}^N L_i \quad (16)$$

where N represents the number of the frame, L_i represents the mean luminance value of frame i .

- Luminance Standard Deviation (LSD):

$$\text{LSD} = \sqrt{\frac{1}{N} \sum_{i=1}^N (L_i - L_{avg})^2} \quad (17)$$

where L_i is the mean luminance of frame i .

A. Comparison with state-of-the-art methods

We quantitatively and qualitatively compare our EAFNet to several state-of-the-art MEF methods including Kalantari [49], AHDR [36], Prabhakar [61], HDR-Transformer [40], SCTNet [43], DomainPlus [39], SAFNet [31], and several state-of-the-art AE methods including HDRFlow [51], LAN-HDR [50], and DeepHDRVideo [19].

Experiments on Prabhakar's datasets and Kalantari's datasets.

TABLE II
CROSS-DATASET EVALUATION ON KALANTARI’S DATASET AND PRABHAKAR’S DATASET. THE BEST RESULTS ARE **HIGHLIGHTED** AND THE SECOND BEST RESULTS ARE UNDERLINED.

Models	2019 AHDRNet	2022 HDR-Trans	2022 DomainPlus	2023 SCTNet	2024 SAFNet	Ours
train on Kalantari’s dataset, test on Prabhakar’s dataset						
PSNR- μ	33.96	34.07	32.64	33.83	38.00	39.26
PSNR-L	32.46	36.62	30.4233	30.95	<u>34.65</u>	35.99
SSIM- μ	0.9601	<u>0.9675</u>	0.9046	0.9584	0.9597	0.9707
SSIM-L	0.9542	<u>0.9656</u>	0.9094	0.9521	<u>0.9793</u>	0.9848
train on Prabhakar’s dataset, test on Kalantari’s dataset						
PSNR- μ	40.03	41.38	41.15	40.88	40.86	42.02
PSNR-L	36.71	39.21	38.18	37.59	37.50	39.38
SSIM- μ	0.9855	0.9890	0.9873	<u>0.9892</u>	0.9882	0.9903
SSIM-L	0.9758	0.9873	0.9837	0.9842	0.9810	<u>0.9870</u>

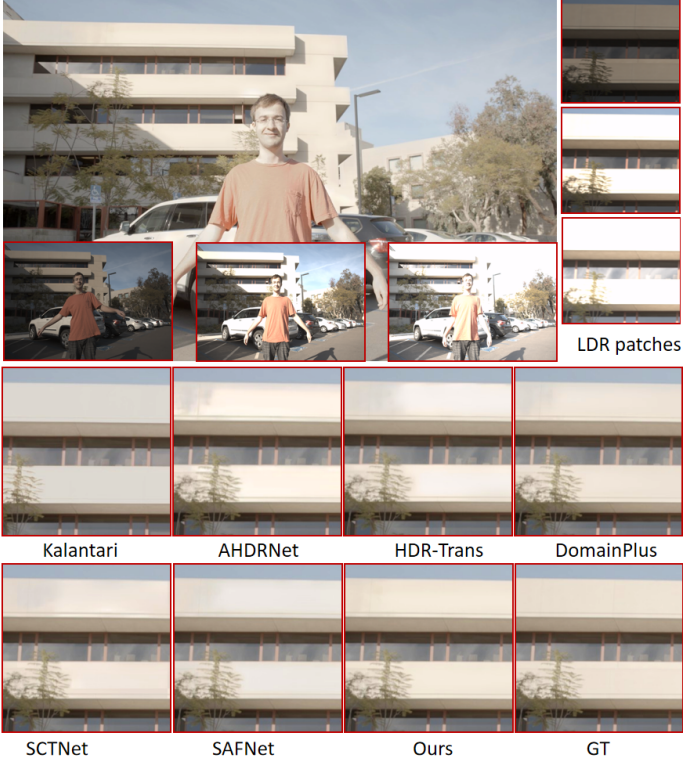


Fig. 6. Visual comparison on Kalantari’s dataset. While other methods suffer from detail loss, overexposed patches, and color inconsistencies, our approach successfully reconstructs overexposed details and preserves natural, consistent color.

Intra-Validation. Our DCS can be viewed as a MEF task, so we conduct a comparison with the state-of-the-art MEF method using the publicly available MEF dataset. The quantitative results on both datasets are shown in Table I, our EAFNet achieves superior performance across all datasets. Specifically, on the Kalantari dataset, our method surpasses the second-best approach in terms of PSNR- μ by 0.08 dB, while on the Prabhakar dataset, it achieves a more substantial improvement of 0.49 dB. The visual comparisons in Fig. 7 illustrate that most existing methods still suffer from noticeable ghosting artifacts. In contrast, the proposed EAFNet effectively mitigates these issues. Moreover, in overexposed regions (Figure 6), we find that the Kalantari method leads to detail loss, while AHDRNet and HDR-Trans exhibit large white overexposed patches in wall areas. Additionally, methods such

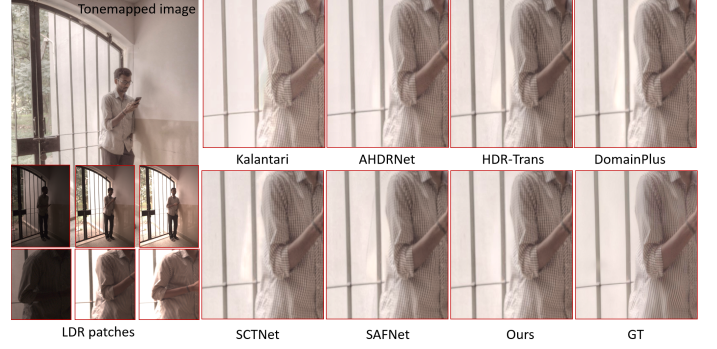


Fig. 7. Visual comparison on Prabhakar’s dataset. Most existing methods suffer from ghosting artifacts, our EAFNet mitigates these issues.

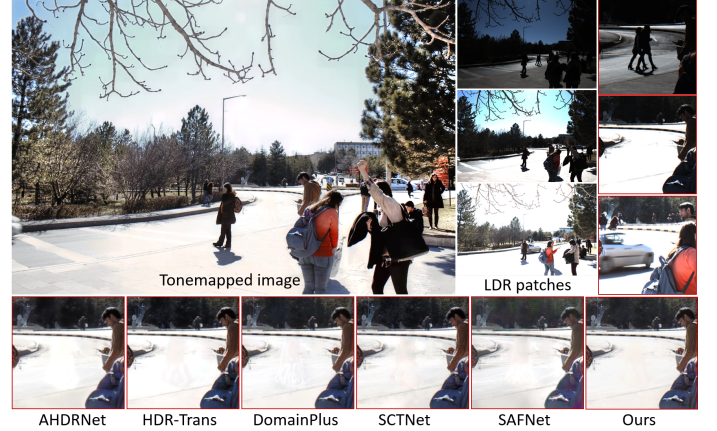


Fig. 8. Visual comparison on Tursun’s dataset. Existing methods often produce artifacts due to luminance contrast between reference and non-reference images, while SAFNet effectively suppresses these artifacts.

as DomainPlus still struggle with color inconsistencies. In contrast, our approach successfully reconstructs most of the overexposed details while preserving natural and consistent color reproduction.

Cross-Validation. The cross-testing on the two datasets serves to mitigate any potential bias and offers a comprehensive understanding of the model’s reliability across varying conditions. As shown in Table II, we achieve superior performance in cross-dataset evaluation, demonstrating the robustness and generalizability of our model.

Unsupervised-dataset. To assess the generalization performance of our SAFNet, we conduct qualitative comparisons on the Sen’s and Tursun’s datasets. As shown in Fig. 8, when there exists a significant luminance contrast between the reference and non-reference images, such as the case where white backgrounds in the reference image correspond to dark content in the non-reference frames, most existing methods tend to produce prominent visual artifacts. In contrast, the proposed SAFNet effectively suppresses artifacts, delivering perceptually plausible HDR reconstructions even in scenes with severe exposure disparity. In Fig. 9, When the reference image is over-exposed and misalignment exists between the reference and non-reference images, methods such as AHDRNet, DominPlus, and SAFNet exhibit incorrect alignment, while HDR-Trans and SCTNet suffer from varying degrees of

TABLE III

COMPARISON ON SELF-CAPTURED VIDEOS. * INDICATES MEF METHODS UNDER THE AE SETUP. THE REPORTED TIME REFERS TO THE INFERENCE TIME FOR A 128×128 PATCH ON A SINGLE RTX 4090 GPU.

	AE setup					MEF setup with DCS				
	21'ICCV	23'ICCV	24'CVPR	23'ICCV	24'ECCV	22'ECCV	22'MM	23'ICCV	24'ECCV	
	Chen	LAN-HDR	HDRFlow	SCTNet*	SAFNet*	HDRTrans	DomainPlus	SCTNet	SAFNet	Ours
LSD	0.1031	0.1003	0.0914	0.1027	0.0976	0.0093	0.0094	0.0093	0.0097	0.0093
t-SSIM	0.5913	0.6879	0.7352	0.6947	0.6862	0.8923	0.8991	0.8868	0.8851	0.9071
L_{avg}	105.02	108.75	113.49	109.23	111.70	111.24	110.41	106.84	111.32	133.16
Runtime(ms)	22.23	21.69	2.6	11.17	3.2	21.6	7.44	11.17	3.2	4.3

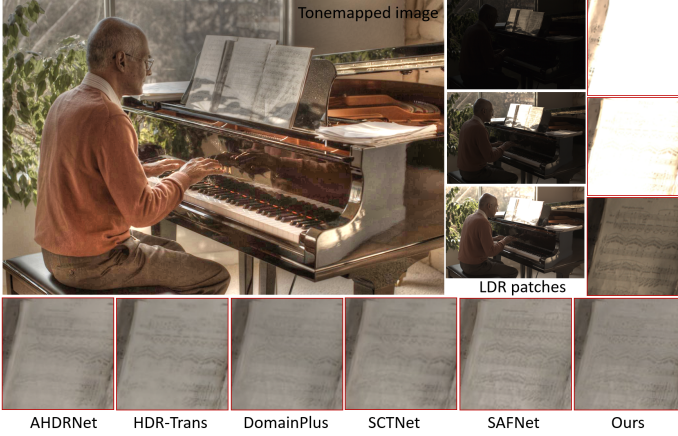


Fig. 9. Visual comparison on Sen’s dataset. Existing methods suffer from misalignment or detail loss when the reference image is over-exposed, while our method reconstructs clearer and more accurate textures.

detail loss. In contrast, our method is capable of reconstructing clearer and more accurate textures.

B. Experiments on self-captured videos

Overview. In this section, we explore the effectiveness of our DCS in real-world scenes and assess the capabilities of the proposed EAFNet in HDR video reconstruction. As detailed in Section III, real video data is captured using dual MV-CS032-10GC industrial cameras. Due to the alternating exposure method’s requirement for continuous alternating exposure frames, direct comparison with our approach under identical settings is not feasible. To ensure a fair comparison, we simultaneously capture two datasets with our system, ensuring minimal scene variation. The first camera captures alternating low, medium, and high exposure sequences, while the second camera continuously captures a medium exposure sequence. The AE method uses the alternating exposure sequence from the first camera as the test dataset, while our dual-camera framework takes low and high-exposure images from the first camera and a continuous medium-exposure sequence from the second. Both cameras have a resolution of 960×540 , and we select nine scenes spanning indoor, outdoor, day, and night conditions, each covering low-light, normal-light, and high-light scenarios with challenges such as high contrast, motion, and occlusion. The gain follows the scene variations, using exposure times of $(-2, 0, 2 \text{ EV})$.

Compare with MEF methods. We compare our method with the state-of-the-art MEF methods including HDR-Transformer

[40], SCTNet [43], DomainPlus [39], and SAFNet [31]. Firstly, we compare the performance of models trained on two different datasets, Prabhakar’s and Kalantari’s. As shown in Fig. 10 (third row), we find that models trained on Kalantari’s dataset exhibit unnatural textures in certain scenes. Therefore, all MEF results are tested using the model trained on Prabhakar’s dataset. During real video capture, complex lighting conditions, camera and object motion, and high-contrast scenes pose significant challenges for video reconstruction. As shown in the first row of Fig. 10, DomainPlus produces motion misalignment artifacts, while SAFNet and SCTNet generate unnatural artifacts in some very dark regions. In contrast, our EAFNet effectively eliminates these artifacts, restoring more natural colors and brightness in darker regions, thus providing more detailed information. The second row of the figure demonstrates that for high-contrast scenes (where reference images are overexposed or areas with white backgrounds correspond to low/high exposure images of dark objects), existing methods fail to eliminate misalignment artifacts. However, our EAFNet can produce more natural reconstruction results, delivering a visually coherent output. The third row shows that our EAFNet provides more detail in the dark region, which leads to high luminance in Table III.

Compare with AE methods. Since the AE method and our method require training on different dataset settings, the AE method is trained on its public dataset following the AE training setup, while our method is trained on the publicly available Prabhakar’s dataset. The models are then tested on our dual-camera dataset. We compare the state-of-the-art AE methods including HDRFlow [51], LAN-HDR [50], and DeepHDRVideo [19]. As shown in Fig. 11 and Table III, for real-world test videos captured in our DCS, the luminance of the video reconstructed using the AE method exhibits abrupt changes, leading to noticeable flickering, which makes it impractical for real-world applications. In contrast, our DCS produces temporally consistent results, which suggests that the proposed system can effectively overcome the challenges of traditional AE methods.

Efficiency Analysis. The overall efficiency of HDR video processing is determined by both the acquisition throughput and the inference speed. Our method specifically targets the acquisition bottleneck by introducing an asynchronous dual-camera design, which decouples the capture of alternate exposure frames from the reference stream. This architecture effectively eliminates the latency caused by long high-exposure frames in traditional single-camera systems, enabling real-time

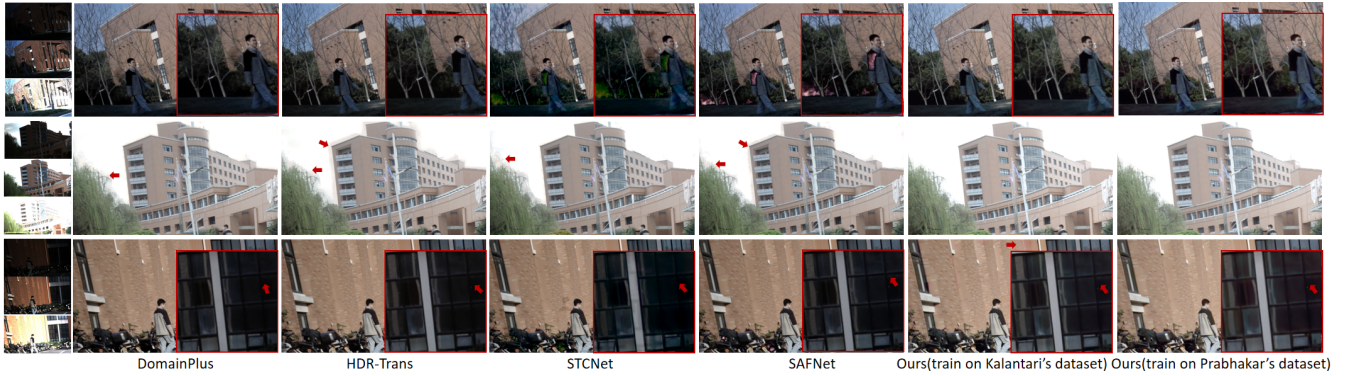


Fig. 10. Visual comparison with MEF methods on self-captured videos. Our EAFNet reduces ghosting from motion (first row) and background misalignment (second row), recovering natural colors and fine details in dark regions (third row).

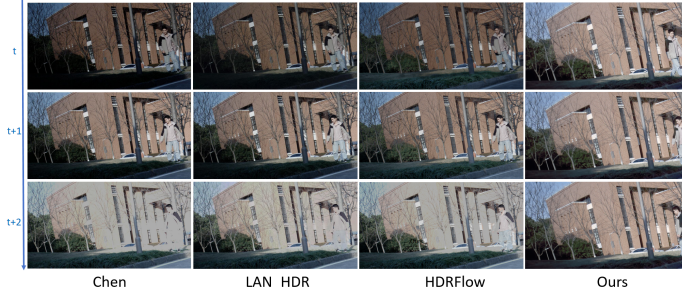


Fig. 11. Visual comparison with AE methods on self-captured video dataset. Our dual-camera system reconstructs HDR video with consistent luminance.

HDR frame acquisition. Although our reconstruction model (EAFNet) is not specifically optimized for real-time inference, as shown in Table III, it still exhibits competitive runtime performance.

Dual-Camera Analysis. The use of a dual-camera system inevitably introduces parallax and temporal misalignment due to the baseline separation and potential desynchronization between the two cameras. In our prototype, the baseline is constrained by mechanical limitations but is minimized to the extent possible. Although some parallax is unavoidable, we find that most MEF-based methods in our system demonstrate reasonable robustness to mild parallax. The training data involves dynamic scenes with moving objects and occlusions, the model thus learns to handle motion-induced spatial misalignments, which share similar characteristics with parallax-related shifts in dual-camera setups. In challenging cases, such as those involving high local contrast, misalignment becomes more difficult to resolve. For instance, in the second row of Figure 10, the presence of strong contrast across exposure frames poses a severe test for existing methods. In typical dynamic scenes with such conditions, most existing approaches struggle to produce satisfactory results. In contrast, our proposed EAFNet effectively mitigates artifacts, preserving detail and structure even under these difficult situations. This robustness is achieved through a combination of a pre-alignment module and a reference-guided fusion strategy, which together reduce visible artifacts even in scenes with high contrast or occlusion.

TABLE IV
T-SSIM COMPARISON UNDER DIFFERENT DUAL-CAMERA DEPLOYMENT SETTINGS

t-SSIM	MEF setup with DCS				
	22'ECCV HDRTrans	22'MM DomainPlus	23'ICCV SCTNet	24'ECCV SAFNet	Ours
ori	0.8923	0.8991	0.8868	0.8851	0.9071
w/o calibration	0.8922	0.8994	0.8872	0.8861	0.9079
random non-reference	0.8926	0.8997	0.8842	0.8848	0.9072
lower frame rate	0.8924	0.8985	0.8871	0.8836	0.9066

TABLE V
THE ABLATION STUDY OF PRE-ALIGNMENT SUBNETWORK AND ASYMMETRIC CROSS-FEATURE FUSION SUBNETWORK ON PRABHAKAR'S DATASETS

pre align		fusion		PSNR- μ	PSNR-L	SSIM- μ	SSIM-L
GLA	EFSM	ACA	$fguide$				
		✓	✓	41.29	39.47	0.9728	0.9888
✓		✓	✓	41.43	39.73	0.9722	0.9890
	✓	✓	✓	41.17	39.33	0.9726	0.9780
✓	✓	✓	✓	41.80	40.14	0.9731	0.9895
✓	✓	CA	✓	41.61	39.80	0.9726	0.9892
✓	✓	✓		41.48	39.79	0.9723	0.9893
✓	✓			41.13	39.12	0.9708	0.9887
				40.81	38.70	0.9703	0.9784

In addition, the system does not rely on precise camera calibration or strict synchronization. The fusion framework is designed to tolerate both geometric misalignment and temporal offset. As shown in Table IV, ablation studies under various calibration conditions and randomized non-reference input orders confirm that the overall reconstruction quality remains stable. Small changes in t-SSIM are mainly due to image cropping rather than alignment failure.

C. Ablation study

In this section, we investigate different components of our system individually to understand the capability of the system and the source of efficiency. Specifically, all quantitative evaluations are performed on Prabhakar's dataset [30].

Global Luminance Alignment. We alter the composition of the input channels and configure four scenarios to investigate the impact of GLA. As shown in Table VI, the first scenario (i.e., our model) exhibits the best performance. The visualization results of the ablation experiments on GLA with Prabhakar's dataset are shown in Fig. 13, in the first row,

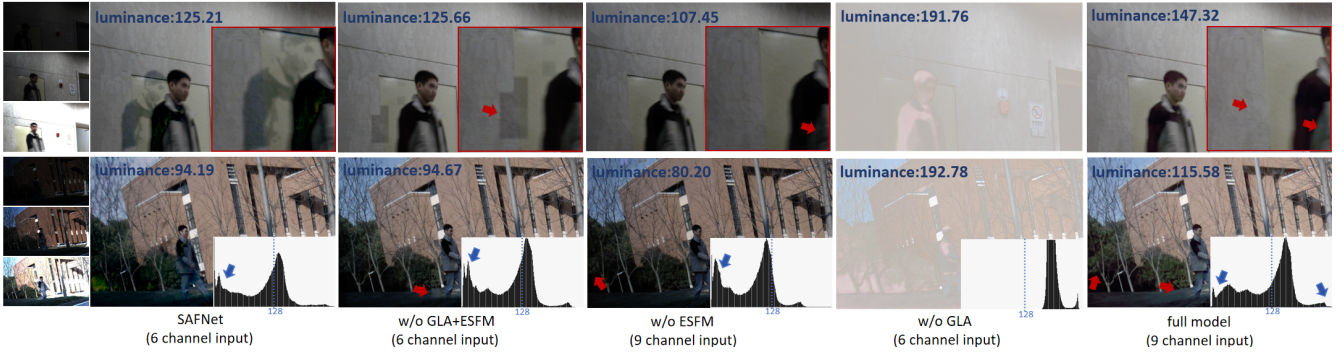


Fig. 12. Visual comparison of ablation on self-captured videos. The integration of GLA and ESFM influences the overall luminance and jointly reduces ghosting while enhancing detail in dark regions. The luminance histograms show that our method increases the visibility of extremely dark areas without causing an increase in high-luminance pixels.



Fig. 13. The contributions of global luminance alignment. Our method effectively suppresses ghosting caused by misalignment and restores more details.

TABLE VI
ABLATION INVESTIGATION ABOUT GLOBAL LUMINANCE ALIGNMENT.

Channels	Original	gamma correction	GLA	PSNR- μ	PSNR- l	SSIM- μ	SSIM- l
9	✓	✓	✓	41.80	40.14	0.9731	0.9895
6	✓	✓	✓	41.17	39.33	0.9726	0.9780
6	✓	✓	✓	41.08	38.97	0.9729	0.9884
6	✓	✓	✓	41.19	39.54	0.9729	0.9882

other variants fail to restore the overexposed details of the window frame. In the second row, ghosting occurs in the overexposed areas outside the window. The introduction of the global luminance alignment method leads to enhanced detail preservation while effectively mitigating undesirable artifacts. **Exposure-Guided Feature Selection Module.** Table V presents the effectiveness of the ESFM. As shown in the first four rows, without global luminance alignment, ESFM not only fails to achieve the expected improvement but also makes a negative optimization in some cases. This can be attributed to the lack of consistent brightness information during the feature selection process, which may lead to a loss of image details. After introducing GLA, ESFM effectively harmonizes the brightness information, mitigating errors caused by brightness variations. As shown in Fig. 12, this integration results in a significant enhancement in detail preservation while the PSNR- μ is increased by 0.37 dB over the baseline. The luminance histograms show that the joint role of GLA and ESFM increases the visibility of extremely dark areas without causing an increase in high-luminance pixels. However, in the absence of ESFM, while some improvements are observed in intra-dataset performance (Table V), introducing GLA alone

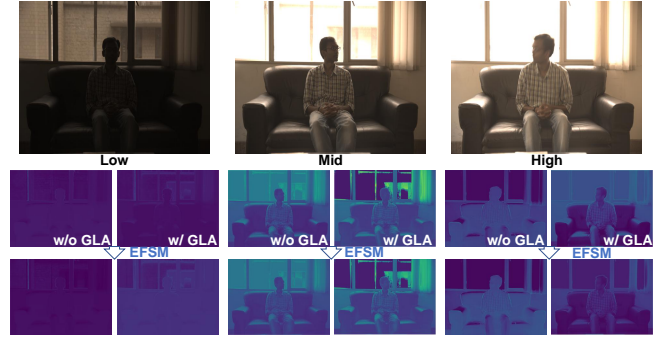


Fig. 14. Visualization of feature maps before and after ESFM. Global luminance alignment is crucial for ESFM, suppressing overexposed areas in the high-exposure input and enhancing underexposed regions in the low-exposure input.

may result in overfitting and suppressing details in high-exposure images. This results in loss of details in dark areas and an overall decrease in image luminance.

We find that feature selection is notably affected by two modulation parameters: feature-guide modulation coefficients and exposure-guide modulation coefficients. To explore this effect more comprehensively, we conduct an in-depth analysis of how varying the modulation coefficient ratios influences performance. As shown in Table VII, we construct five different networks with varying modulation coefficient ratios. Among these, the 2:1 ratio achieves the highest PSNR- μ , indicating optimal performance under this configuration. As shown in Fig. 14, the proposed GLA and ESFM work collaboratively to fully explore exposure information and enhance meaningful details. Specifically, the shadow details in low-exposure features are enhanced, while the overexposed regions in high-exposure features are suppressed.

Asymmetric Cross-feature Fusion Subnetwork. As shown in Table V, replacing the asymmetric cross-feature fusion subnetwork with a generally used attention subnetwork [36] (line 7) results in a 0.67 dB drop in PSNR- μ . Fig. 16 and Fig. 15 further confirms that our method effectively mitigates misalignment artifacts. Additionally, we evaluate the role of the asymmetric cross-attention (ACA) by comparing it with cross-attention (CA) mechanism. The ACA improves PSNR-

TABLE VII
EXPERIMENTS ON CHANGING THE PROPORTIONS IN EXPOSURE-GUIDED
FEATURE SELECTION MODULE

Proportions	PSNR- μ	PSNR- l	SSIM- μ	SSIM- l
1:2	41.41	39.66	0.97281	0.97907
1:1	41.43	39.70	0.97284	0.98918
2:1	41.80	40.14	0.97311	0.98953
4:1	41.68	40.00	0.97251	0.98934
8:1	41.72	40.02	0.97255	0.98938

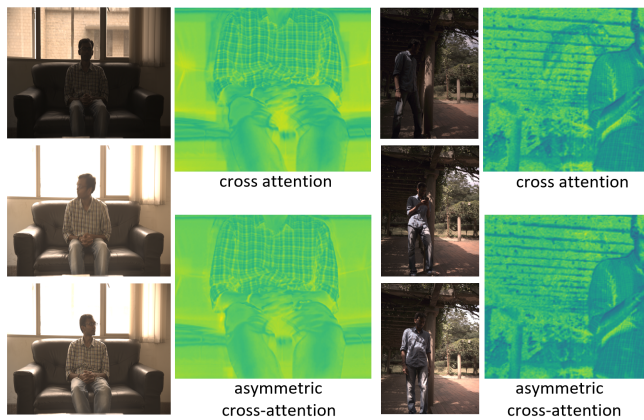


Fig. 15. Visual comparison of asymmetric cross-attention and cross-attention. Our method reduces misalignment artifacts.

TABLE VIII
VISUAL COMPARISON OF THE SEPARATE EFFECTS OF RESTORATION
NETWORK.

model	PSNR- μ	PSNR- L	SSIM- μ	SSIM- L
baseline	40.81	38.60	0.97192	0.98813
w/o mutil-scale	41.58	39.86	0.97249	0.98911
w/o DWT	41.71	40.04	0.97286	0.98937
Ours	41.80	40.14	0.97311	0.98953

μ by 0.19 dB (line 5). The cross-scale guidance features f_{guide} further enhance fusion accuracy, reducing artifacts and contributing to a 0.32 dB gain in PSNR- μ .

Restoration Subnetwork In this section, we conduct ablation experiments to evaluate the role of the frequency-domain design and multiscale structure in HDR reconstruction. As shown in Table VIII, the baseline model (merging network in AHDNet) achieves a PSNR- μ of 40.81 and an SSIM- μ of 0.9719. First, we remove the frequency-domain design, and the results show that the PSNR- μ dropped by 0.09. Next, we perform an ablation experiment on the multiscale structure by removing it. The results indicate that, without the multiscale structure, the PSNR- μ decreased by 0.22. Our full model, which incorporates both the frequency-domain design and multiscale structure, yields the highest performance, achieving a PSNR- μ of 41.80 and an SSIM- μ of 0.97311.

VI. CONCLUSION

In this work, we propose a dual-camera system (DCS) to mitigate the temporal inconsistency with AE methods,

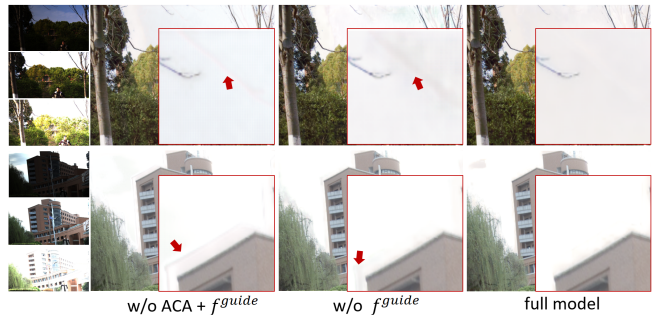


Fig. 16. Visual comparison of ablation on self-captured videos. Our method reduces most ghosting artifacts.

and existing MEF methods can be seamlessly extended to our system with temporally consistent output. In addition, we introduce an exposure adaptive fusion network with two novel subnetworks to provide a more stable and efficient solution for video HDR reconstruction. Experimental results demonstrate that our approach outperforms existing methods, offering stable performance and high-quality reconstruction in complex real-world video environments. Our dual-camera framework provides a promising direction for real-time HDR video capture.

REFERENCES

- [1] P. E. Debevec and J. Malik, "Recovering high dynamic range radiance maps from photographs," in *ACM SIGGRAPH 2008 classes*, 2008, pp. 1–10.
- [2] K. Jacobs, C. Loscos, and G. Ward, "Automatic high-dynamic range image generation for dynamic scenes," *IEEE Computer Graphics and Applications*, vol. 28, no. 2, pp. 84–93, 2008.
- [3] H. Li, K. Ma, H. Yong, and L. Zhang, "Fast multi-scale structural patch decomposition for multi-exposure image fusion," *IEEE Transactions on Image Processing*, vol. 29, pp. 5805–5816, 2020.
- [4] L. Bogoni, "Extending dynamic range of monochrome and color images through fusion," in *Proceedings 15th International Conference on Pattern Recognition. ICPR-2000*, vol. 3. IEEE, 2000, pp. 7–12.
- [5] P. Sen, N. K. Kalantari, M. Yaesoubi, S. Darabi, D. B. Goldman, and E. Shechtman, "Robust patch-based hdr reconstruction of dynamic scenes," *ACM Trans. Graph.*, vol. 31, no. 6, pp. 203–1, 2012.
- [6] J. Kronander, S. Gustavson, G. Bonnet, A. Ynnerman, and J. Unger, "A unified framework for multi-sensor hdr video reconstruction," *Signal Processing: Image Communication*, vol. 29, no. 2, pp. 203–215, 2014.
- [7] M. McGuire, W. Matusik, H. Pfister, B. Chen, J. F. Hughes, and S. K. Nayar, "Optical splitting trees for high-precision monocular imaging," *IEEE Computer Graphics and Applications*, vol. 27, no. 2, pp. 32–42, 2007.
- [8] M. D. Tocci, C. Kiser, N. Tocci, and P. Sen, "A versatile hdr video production system," *ACM Transactions on Graphics (TOG)*, vol. 30, no. 4, pp. 1–10, 2011.
- [9] I. Choi, S.-H. Baek, and M. H. Kim, "Reconstructing interlaced high-dynamic-range video using joint learning," *IEEE Transactions on Image Processing*, vol. 26, no. 11, pp. 5353–5366, 2017.
- [10] F. Heide, M. Steinberger, Y.-T. Tsai, M. Rouf, D. Pajkak, D. Reddy, O. Gallo, J. Liu, W. Heidrich, K. Egiazarian *et al.*, "Flexisp: A flexible camera image processing framework," *ACM Transactions on Graphics (ToG)*, vol. 33, no. 6, pp. 1–13, 2014.
- [11] H. Zhao, B. Shi, C. Fernandez-Cull, S.-K. Yeung, and R. Raskar, "Unbounded high dynamic range photography using a modulo camera," in *2015 IEEE International Conference on Computational Photography (ICCP)*. IEEE, 2015, pp. 1–10.
- [12] J. Han, C. Zhou, P. Duan, Y. Tang, C. Xu, C. Xu, T. Huang, and B. Shi, "Neuromorphic camera guided high dynamic range imaging," in *Proceedings of the IEEE/CVF Conference on Computer Vision and Pattern Recognition*, 2020, pp. 1730–1739.

- [13] K. Jacobs, C. Loscos, and G. Ward, "Automatic high-dynamic range image generation for dynamic scenes," *IEEE Computer Graphics and Applications*, vol. 28, no. 2, pp. 84–93, 2008.
- [14] T.-H. Min, R.-H. Park, and S. Chang, "Histogram based ghost removal in high dynamic range images," in *2009 IEEE International Conference on Multimedia and Expo*. IEEE, 2009, pp. 530–533.
- [15] K. Ma, H. Li, H. Yong, Z. Wang, D. Meng, and L. Zhang, "Robust multi-exposure image fusion: a structural patch decomposition approach," *IEEE Transactions on Image Processing*, vol. 26, no. 5, pp. 2519–2532, 2017.
- [16] S. B. Kang, M. Uyttendaele, S. Winder, and R. Szeliski, "High dynamic range video," *ACM Transactions on Graphics (TOG)*, vol. 22, no. 3, pp. 319–325, 2003.
- [17] S. Mangiat and J. Gibson, "High dynamic range video with ghost removal," in *Applications of digital image processing XXXIII*, vol. 7798. SPIE, 2010, pp. 307–314.
- [18] Y. Gryaditskaya, T. Pouli, E. Reinhard, K. Myszkowski, and H.-P. Seidel, "Motion aware exposure bracketing for hdr video," in *Computer Graphics Forum*, vol. 34, no. 4. Wiley Online Library, 2015, pp. 119–130.
- [19] G. Chen, C. Chen, S. Guo, Z. Liang, K.-Y. K. Wong, and L. Zhang, "Hdr video reconstruction: A coarse-to-fine network and a real-world benchmark dataset," in *Proceedings of the IEEE/CVF international conference on computer vision*, 2021, pp. 2502–2511.
- [20] J. Cui, W. Jiang, Z. Peng, Z. Pan, and Z. Cao, "Exposure completing for temporally consistent neural high dynamic range video rendering," in *Proceedings of the 32nd ACM International Conference on Multimedia*, 2024, pp. 10027–10035.
- [21] J. Hu, O. Gallo, K. Pulli, and X. Sun, "Hdr deghosting: How to deal with saturation?" in *Proceedings of the IEEE Conference on Computer Vision and Pattern Recognition*, 2013, pp. 1163–1170.
- [22] D. Hafner, O. Demetz, and J. Weickert, "Simultaneous hdr and optic flow computation," in *2014 22nd International Conference on Pattern Recognition*. IEEE, 2014, pp. 2065–2070.
- [23] T. Grosch *et al.*, "Fast and robust high dynamic range image generation with camera and object movement," *Vision, Modeling and Visualization, RWTH Aachen*, vol. 277284, no. 3, p. 2, 2006.
- [24] Y. S. Heo, K. M. Lee, S. U. Lee, Y. Moon, and J. Cha, "Ghost-free high dynamic range imaging," in *Asian Conference on Computer Vision*. Springer, 2010, pp. 486–500.
- [25] W. Zhang and W.-K. Cham, "Gradient-directed multiexposure composition," *IEEE Transactions on Image Processing*, vol. 21, no. 4, pp. 2318–2323, 2011.
- [26] C. Lee, Y. Li, and V. Monga, "Ghost-free high dynamic range imaging via rank minimization," *IEEE signal processing letters*, vol. 21, no. 9, pp. 1045–1049, 2014.
- [27] T.-H. Oh, J.-Y. Lee, Y.-W. Tai, and I. S. Kweon, "Robust high dynamic range imaging by rank minimization," *IEEE transactions on pattern analysis and machine intelligence*, vol. 37, no. 6, pp. 1219–1232, 2014.
- [28] N. K. Kalantari, R. Ramamoorthi *et al.*, "Deep high dynamic range imaging of dynamic scenes," *ACM Trans. Graph.*, vol. 36, no. 4, pp. 144–1, 2017.
- [29] F. Peng, M. Zhang, S. Lai, H. Tan, and S. Yan, "Deep hdr reconstruction of dynamic scenes," in *2018 IEEE 3rd International Conference on Image, Vision and Computing (ICIVC)*. IEEE, 2018, pp. 347–351.
- [30] K. R. Prabhakar, R. Arora, A. Swaminathan, K. P. Singh, and R. V. Babu, "A fast, scalable, and reliable deghosting method for extreme exposure fusion," in *2019 IEEE International Conference on Computational Photography (ICCP)*. IEEE, 2019, pp. 1–8.
- [31] L. Kong, B. Li, Y. Xiong, H. Zhang, H. Gu, and J. Chen, "Safnet: Selective alignment fusion network for efficient hdr imaging," in *European Conference on Computer Vision*. Springer, 2024, pp. 256–273.
- [32] S. Wu, J. Xu, Y.-W. Tai, and C.-K. Tang, "End-to-end deep hdr imaging with large foreground motions," in *European Conference on Computer Vision*, vol. 1, no. 2, 2018.
- [33] Q. Yan, B. Wang, L. Zhang, J. Zhang, Z. You, Q. Shi, and Y. Zhang, "Towards accurate hdr imaging with learning generator constraints," *Neurocomputing*, vol. 428, pp. 79–91, 2021.
- [34] Y. Niu, J. Wu, W. Liu, W. Guo, and R. W. Lau, "Hdr-gan: Hdr image reconstruction from multi-exposed ldr images with large motions," *IEEE Transactions on Image Processing*, vol. 30, pp. 3885–3896, 2021.
- [35] R. Li, C. Wang, J. Wang, G. Liu, H.-Y. Zhang, B. Zeng, and S. Liu, "Uphdr-gan: Generative adversarial network for high dynamic range imaging with unpaired data," *IEEE Transactions on Circuits and Systems for Video Technology*, vol. 32, no. 11, pp. 7532–7546, 2022.
- [36] Q. Yan, D. Gong, Q. Shi, A. v. d. Hengel, C. Shen, I. Reid, and Y. Zhang, "Attention-guided network for ghost-free high dynamic range imaging," in *Proceedings of the IEEE/CVF Conference on Computer Vision and Pattern Recognition*, 2019, pp. 1751–1760.
- [37] Z. Liu, W. Lin, X. Li, Q. Rao, T. Jiang, M. Han, H. Fan, J. Sun, and S. Liu, "Adnet: Attention-guided deformable convolutional network for high dynamic range imaging," in *Proceedings of the IEEE/CVF Conference on Computer Vision and Pattern Recognition*, 2021, pp. 463–470.
- [38] J. Chen, Z. Yang, T. N. Chan, H. Li, J. Hou, and L.-P. Chau, "Attention-guided progressive neural texture fusion for high dynamic range image restoration," *IEEE Transactions on Image Processing*, vol. 31, pp. 2661–2672, 2022.
- [39] B. Zheng, X. Pan, H. Zhang, X. Zhou, G. Slabaugh, C. Yan, and S. Yuan, "Domainplus: Cross transform domain learning towards high dynamic range imaging," in *Proceedings of the 30th ACM International Conference on Multimedia*, 2022, pp. 1954–1963.
- [40] Z. Liu, Y. Wang, B. Zeng, and S. Liu, "Ghost-free high dynamic range imaging with context-aware transformer," in *European Conference on Computer Vision*. Springer, 2022, pp. 344–360.
- [41] R. Chen, B. Zheng, H. Zhang, Q. Chen, C. Yan, G. Slabaugh, and S. Yuan, "Improving dynamic hdr imaging with fusion transformer," in *Proceedings of the AAAI Conference on Artificial Intelligence*, vol. 37, no. 1, 2023, pp. 340–349.
- [42] Q. Yan, W. Chen, S. Zhang, Y. Zhu, J. Sun, and Y. Zhang, "A unified hdr imaging method with pixel and patch level," in *Proceedings of the IEEE/CVF Conference on Computer Vision and Pattern Recognition*, 2023, pp. 22 211–22 220.
- [43] S. Tel, Z. Wu, Y. Zhang, B. Heyrman, C. Demonceaux, R. Timofte, and D. Ginhac, "Alignment-free hdr deghosting with semantics consistent transformer," in *2023 IEEE/CVF International Conference on Computer Vision (ICCV)*. IEEE Computer Society, 2023, pp. 12 790–12 799.
- [44] X. Dong, X. Hu, W. Li, X. Wang, and Y. Wang, "Miehdr cnn: Main image enhancement based ghost-free high dynamic range imaging using dual-lens systems," in *Proceedings of the AAAI Conference on Artificial Intelligence*, vol. 35, no. 2, 2021, pp. 1264–1272.
- [45] W. Li, T. Cao, C. Liu, X. Tian, Y. Li, X. Wang, and X. Dong, "Dual-lens hdr using guided 3d exposure cnn and guided denoising transformer," *ACM Transactions on Multimedia Computing, Communications and Applications*, vol. 19, no. 5, pp. 1–20, 2023.
- [46] S. K. Nayar and T. Mitsunaga, "High dynamic range imaging: Spatially varying pixel exposures," in *Proceedings IEEE Conference on Computer Vision and Pattern Recognition. CVPR 2000 (Cat. No. PR00662)*, vol. 1. IEEE, 2000, pp. 472–479.
- [47] S. Mangiat and J. Gibson, "Spatially adaptive filtering for registration artifact removal in hdr video," in *2011 18th IEEE International Conference on Image Processing*. IEEE, 2011, pp. 1317–1320.
- [48] Y. Li, C. Lee, and V. Monga, "A maximum a posteriori estimation framework for robust high dynamic range video synthesis," *IEEE Transactions on Image Processing*, vol. 26, no. 3, pp. 1143–1157, 2016.
- [49] N. K. Kalantari and R. Ramamoorthi, "Deep hdr video from sequences with alternating exposures," in *Computer graphics forum*, vol. 38, no. 2. Wiley Online Library, 2019, pp. 193–205.
- [50] H. Chung and N. I. Cho, "Lan-hdr: Luminance-based alignment network for high dynamic range video reconstruction," in *Proceedings of the IEEE/CVF International Conference on Computer Vision*, 2023, pp. 12 760–12 769.
- [51] G. Xu, Y. Wang, J. Gu, T. Xue, and X. Yang, "Hdrflow: Real-time hdr video reconstruction with large motions," in *Proceedings of the IEEE/CVF Conference on Computer Vision and Pattern Recognition*, 2024, pp. 24 851–24 860.
- [52] Z. Zhang, "A flexible new technique for camera calibration," *IEEE Transactions on pattern analysis and machine intelligence*, vol. 22, no. 11, pp. 1330–1334, 2002.
- [53] N. K. Kalantari, R. Ramamoorthi *et al.*, "Deep high dynamic range imaging of dynamic scenes," *ACM Trans. Graph.*, vol. 36, no. 4, pp. 144–1, 2017.
- [54] Z. Liu, Y. Lin, Y. Cao, H. Hu, Y. Wei, Z. Zhang, S. Lin, and B. Guo, "Swin transformer: Hierarchical vision transformer using shifted windows," in *Proceedings of the IEEE/CVF international conference on computer vision*, 2021, pp. 10 012–10 022.
- [55] B. Zheng, Y. Chen, X. Tian, F. Zhou, and X. Liu, "Implicit dual-domain convolutional network for robust color image compression artifact reduction," *IEEE Transactions on Circuits and Systems for Video Technology*, vol. 30, no. 11, pp. 3982–3994, 2019.
- [56] B. Zheng, S. Yuan, C. Yan, X. Tian, J. Zhang, Y. Sun, L. Liu, A. Leonardis, and G. Slabaugh, "Learning frequency domain priors for

- image demoireing,” *IEEE Transactions on Pattern Analysis and Machine Intelligence*, vol. 44, no. 11, pp. 7705–7717, 2021.
- [57] D. P. Kingma and J. Ba, “Adam: A method for stochastic optimization,” *arXiv preprint arXiv:1412.6980*, 2014.
 - [58] O. T. Tursun, A. O. Akyüz, A. Erdem, and E. Erdem, “An objective deghosting quality metric for hdr images,” in *Computer Graphics Forum*, vol. 35, no. 2. Wiley Online Library, 2016, pp. 139–152.
 - [59] Z. Wang, A. C. Bovik, H. R. Sheikh, and E. P. Simoncelli, “Image quality assessment: from error visibility to structural similarity,” *IEEE transactions on image processing*, vol. 13, no. 4, pp. 600–612, 2004.
 - [60] R. Mantiuk, K. J. Kim, A. G. Rempel, and W. Heidrich, “Hdr-vdp-2: A calibrated visual metric for visibility and quality predictions in all luminance conditions,” *ACM Transactions on graphics (TOG)*, vol. 30, no. 4, pp. 1–14, 2011.
 - [61] K. R. Prabhakar, S. Agrawal, D. K. Singh, B. Ashwath, and R. V. Babu, “Towards practical and efficient high-resolution hdr deghosting with cnn,” in *Computer Vision–ECCV 2020: 16th European Conference, Glasgow, UK, August 23–28, 2020, Proceedings, Part XXI 16*. Springer, 2020, pp. 497–513.